

# SCUBA and Spitzer observations of the Taurus molecular cloud – pulling the bull’s tail

D. Nutter<sup>\*</sup>, J. M. Kirk, D. Stamatellos, D. Ward-Thompson

*Department of Physics and Astronomy, Cardiff University, Queens Buildings, Cardiff, CF24 3AA*

29 October 2018

## ABSTRACT

We present continuum data from the Submillimetre Common-User Bolometer Array (SCUBA) on the James Clerk Maxwell Telescope (JCMT), and the Mid-Infrared Photometer for Spitzer (MIPS) on the Spitzer Space Telescope, at submillimetre and infrared wavelengths respectively. We study the Taurus molecular cloud 1 (TMC1), and in particular the region of the Taurus Molecular Ring (TMR). In the continuum data we see no real evidence for a ring, but rather we see one side of it only, appearing as a filament. We name the filament ‘the bull’s tail’. The filament is seen in emission at 850, 450 and 160  $\mu\text{m}$ , and in absorption at 70  $\mu\text{m}$ . We compare the data with archive data from the Infra-Red Astronomical Satellite (IRAS) at 12, 25, 60, 100  $\mu\text{m}$ , in which the filament is also seen in absorption. We find that the emission from the filament consists of two components: a narrow, cold ( $\sim 8$  K), central core; and a broader, slightly warmer ( $\sim 12$  K), shoulder of emission. We use a radiative transfer code to model the filament’s appearance, either in emission or absorption, simultaneously at each of the different wavelengths. Our best fit model uses a Plummer-like density profile and a homogeneous interstellar dust grain population. Unlike previous work on a similar, but different filament in Taurus, we require no grain coagulation to explain our data.

**Key words:** stars: formation – stars: pre-main-sequence – ISM: clouds – ISM: dust, extinction – ISM individual:Taurus

## 1 INTRODUCTION

The Taurus molecular cloud is one of the nearest star forming regions, at a distance of  $\sim 140$  pc (Elias 1978). As such it has often been the target of observational studies into the processes of molecular cloud evolution and star formation. The large scale structure of the molecular cloud has been mapped using the emission from CO (Ungerechts & Thaddeus 1987; Onishi et al. 1996; Goldsmith et al. 2005), and also the extinction of starlight (Cambr esy 1999; Padoan, Cambr esy, & Langer 2002; Dobashi et al. 2005).

The cloud has been mapped to study the formation mechanism of molecular clouds (Ballesteros-Paredes, Hartmann, & V azquez-Semadeni 1999), and the nature of the turbulence that pervades them (see review by Elmegreen & Scalo 2004). On smaller scales, detailed studies of the densest regions of the cloud have greatly increased our knowledge of the star-formation process itself (Ward-Thompson et al. 2000; Motte & Andr e 2001; Onishi et al. 2002; Duch ene et al. 2004; Kirk, Ward-Thompson, & Andr e 2005).

Taurus differs from other nearby sites of star formation, in that it is forming stars in a quiescent manner. There are no newly formed, massive stars injecting energy into the cloud; and compared to more dynamic star-formation regions like Orion or  $\rho$ -Ophiuchus, each of the star-forming cores are widely separated (e.g. Motte, Andr e, & Neri 1998; Ward-Thompson, Motte, & Andr e 1999). The cloud also appears to have a core mass function which differs from that found in other regions (Onishi et al. 2002; Goodwin, Whitworth, & Ward-Thompson 2004).

The far-infrared and submillimetre continuum represent an efficient means of detecting cold star-forming cores in molecular clouds, even in energetic regions such as Orion (Ward-Thompson et al. 1995; Bontemps, Ward-Thompson, & Andr e 1996). Figure 1 shows the Taurus molecular cloud as seen in extinction (Dobashi et al. 2005), with the contours showing the visual extinctions of  $A_v=1$  and  $A_v=5$ . A number of the Lynds clouds which are associated with the Taurus molecular cloud are labelled.

The majority of the cloud has been mapped in the far-infrared by Spitzer (G udel, Padgett, & Dougados 2007, for more details, see Section 2.2). The region mapped by Spitzer is outlined in white on Figure 1. A somewhat smaller region,

<sup>\*</sup> E-mail: David.Nutter@astro.cf.ac.uk

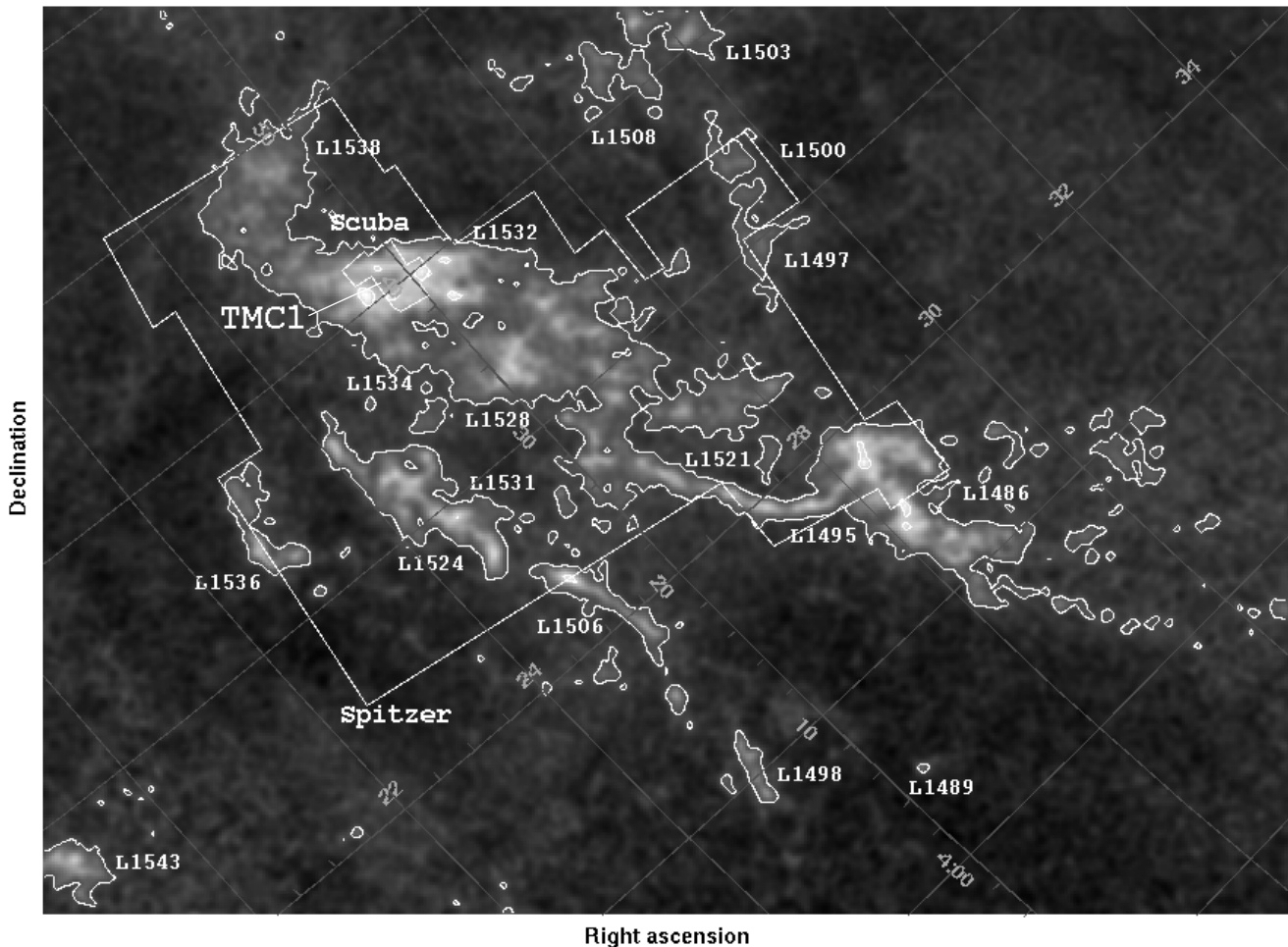


**Figure 1.** The Taurus molecular cloud seen in extinction (Dobashi et al. 2005). The  $A_v=1$  and  $A_v=5$  contours are shown. TMC1 is marked, as are a number of Lynds dark clouds (Lynds 1962). The outlines of the regions mapped by MIPS at  $160\mu\text{m}$  (large box), and SCUBA at  $850\mu\text{m}$  (small box), are shown. The SCUBA data are centred around TMC1.

centred on Taurus molecular cloud 1 (TMC1), has been mapped by SCUBA on the JCMT (see Section 2.1). This smaller region is also outlined in white on Figure 1. The densest part of the cloud is TMC1. Together with Heiles Cloud 2 (HCL2; Heiles 1968) this makes up the Taurus Molecular Ring (TMR) (see Tóth et al. 2004).

Figures 2(a) and (b) show the region around TMC1 at 160 and  $850\mu\text{m}$  respectively, with the brighter components of Heiles Cloud 2 and TMC1 marked. In addition, the approximate locus of the TMR is also marked. For more details about these data, see Section 2. However, we note here that the molecular ring is not really seen in the continuum. Instead, we see a filament in the eastern half and a series of point-like and extended sources scattered roughly around the western half. We therefore challenge the existence of the ring as a single coherent entity, as that is not what is seen in these data. We here name the filament ‘the bull’s tail’.

In this paper, we present a study of a portion of TMC1 using infrared and submillimetre data between 12 and  $850\mu\text{m}$ . This range of wavelengths straddles the peak of the spectral energy distribution (SED) for the cold dust that is found in the densest regions of molecular clouds. Infrared and sub-mm data are therefore a powerful tool for

breaking the degeneracy of temperature and density that is present when only sub-mm data are considered.

## 2 OBSERVATIONS

### 2.1 SCUBA Data

The submillimetre data presented in this study were obtained using the Submillimetre Common User Bolometer Array (SCUBA – Holland et al. 1999) on the James Clerk Maxwell Telescope (JCMT). SCUBA takes observations at 450 and  $850\mu\text{m}$  simultaneously through the use of a dichroic beam-splitter. The telescope has a resolution of 8 arcsec at  $450\mu\text{m}$  and 14 arcsec at  $850\mu\text{m}$ . The data presented here were acquired from the JCMT data archive, operated by the Canadian Astronomy Data Centre. A sub-set of these data has been published previously (Schnee et al. 2007), though all of the data have been re-reduced by us using a consistent method for the purposes of this study.

The observations were carried out over 12 separate nights between December 1998 and January 2005 using the scan-map observing mode. A scan-map is made by scanning the array across the sky, using a scan direction of  $15.5^\circ$  from

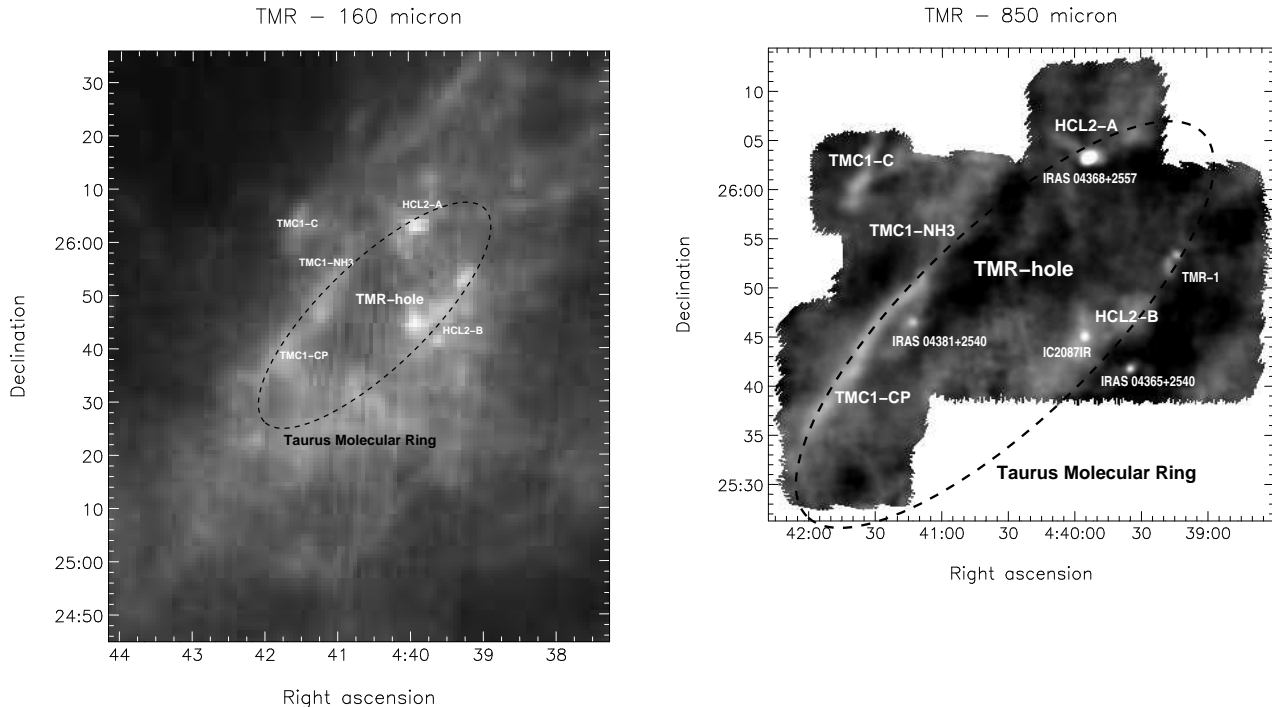


**Figure 2.** A close-up of the TMC1 region at (a) 160  $\mu\text{m}$ , and (b) 850  $\mu\text{m}$ . The bright components of TMC1 and HCL2 are marked (TMC1-CP and TMC1-NH3 refer to the cyclopolyne and ammonia peaks respectively – Olano, Walmsley, & Wilson 1988). Some bright IRAS sources are also marked. The approximate locus of the TMR is shown as a dashed line. The ring structure is not very clear in the continuum images. Instead we see a filament coincident with the eastern portion of the ring, and simply a collection of point sources and clumps in the western half. We here name the filament ‘the bull’s tail’.

the axis of the array in order to achieve Nyquist sampling. The array is rastered across the sky to build up a map several arcminutes in extent.

Time-dependent variations in the sky emission were removed by chopping the secondary mirror at 7.8 Hz. The size of a scan-map is larger than the chop throw, therefore each source in the map appears as a positive and a negative feature. In order to remove this dual-beam function, each region is mapped six times, using chop throws of 30, 44 and 68 arcsec in both RA and Dec (Emerson 1995). The dual-beam function is removed from each map in Fourier space by dividing each map by the Fourier transform of the dual-beam function, which is a sinusoid. The multiple chop-throws allow for cleaner removal of the dual beam function in Fourier space. The maps are then combined, weighting each map to minimise the noise introduced at the spatial frequencies that correspond to zeroes in the sinusoids. Finally the map is inverse Fourier transformed, at which point it no longer contains the negative sources (Jenness & Lightfoot 2000).

The submillimetre zenith opacity at 450 and 850  $\mu\text{m}$  was determined using the ‘skydip’ method and by comparison with polynomial fits to the 1.3 mm sky opacity data, measured at the Caltech Submillimeter Observatory (Archibald et al. 2002). The sky opacity at 850  $\mu\text{m}$  varied from 0.18 to 0.59, with a median value of 0.27. These correspond to a 450  $\mu\text{m}$  opacity range of 0.81 to 3.5, and a median value of 1.4.

The data were reduced in the normal way using the SCUBA User Reduction Facility, SURF (Jenness & Lightfoot 2000). Noisy bolometers were removed by eye, and the baselines, caused by chopping onto

sky with a different level of emission, were removed using the *MEDIAN* filter. Calibration was performed using observations of the planets Uranus and Mars, and the secondary calibrator CRL618 (Sandell 1994) taken during each shift. We estimate that the absolute calibration uncertainty is  $\pm 5\%$  at 850  $\mu\text{m}$  and  $\pm 15\%$  at 450  $\mu\text{m}$ , based on the consistency and reproducibility of the calibration from map to map. The resolution of the SCUBA data was degraded using a Gaussian smoothing routine to a 45 arcsec beam, to allow a direct comparison of these data with the Spitzer data.

## 2.2 MIPS Data

The Multiband Imaging Photometer for Spitzer (MIPS; Rieke et al. 2004) is the far-IR camera on board the Spitzer Space Telescope (Werner et al. 2004). It operates at 24, 70 and 160  $\mu\text{m}$ , and has a diffraction-limited resolution of 6, 18 and 40 arcsec respectively at the three wavelengths.

Spitzer legacy surveys have been used to map most of the star-forming regions within 0.5 kpc and hence produce a complete mid-infrared record of the nearby large molecular clouds. These legacy surveys include ‘Cores to Disks’ (c2d – Evans et al. 2003), the ‘Spitzer Gould Belt Legacy Survey’ (Allen et al. 2007), and the ‘Taurus-2 Spitzer Legacy Project’<sup>1</sup> (Güdel, Padgett, & Dougados 2007). The Spitzer archive data used here were observed as part of the ‘Taurus-2 Spitzer Legacy Project’.

<sup>1</sup> <http://spider.ipac.caltech.edu/staff/dlp/taurus/>

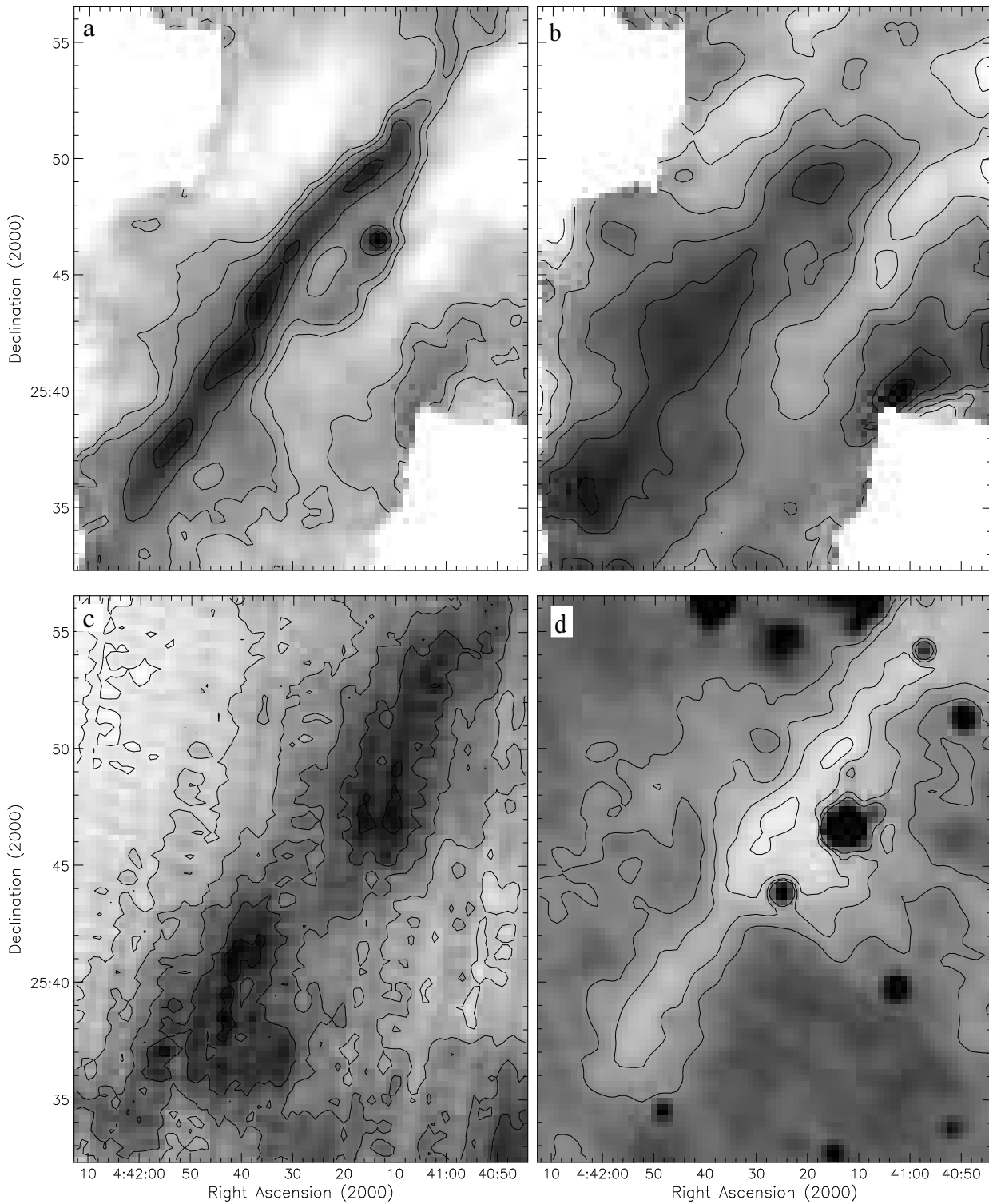


**Figure 3.** An even closer view of the bull's tail filament at (a) 850  $\mu\text{m}$ , (b) 450  $\mu\text{m}$ , (c) 160  $\mu\text{m}$ , and (d) 70  $\mu\text{m}$ . The filament is seen in emission at the three long wavelengths, and in absorption at 70  $\mu\text{m}$ . Each of the maps has been smoothed to match the 45-arcsec angular resolution of the MIPS 160- $\mu\text{m}$  data. The remaining differences in the width of the filament are therefore intrinsic to the source itself. The filament is narrowest at 850 and 70  $\mu\text{m}$ , where there is good agreement between the emission at 850 and absorption at 70  $\mu\text{m}$ . The filament appears broader at the other two wavelengths.

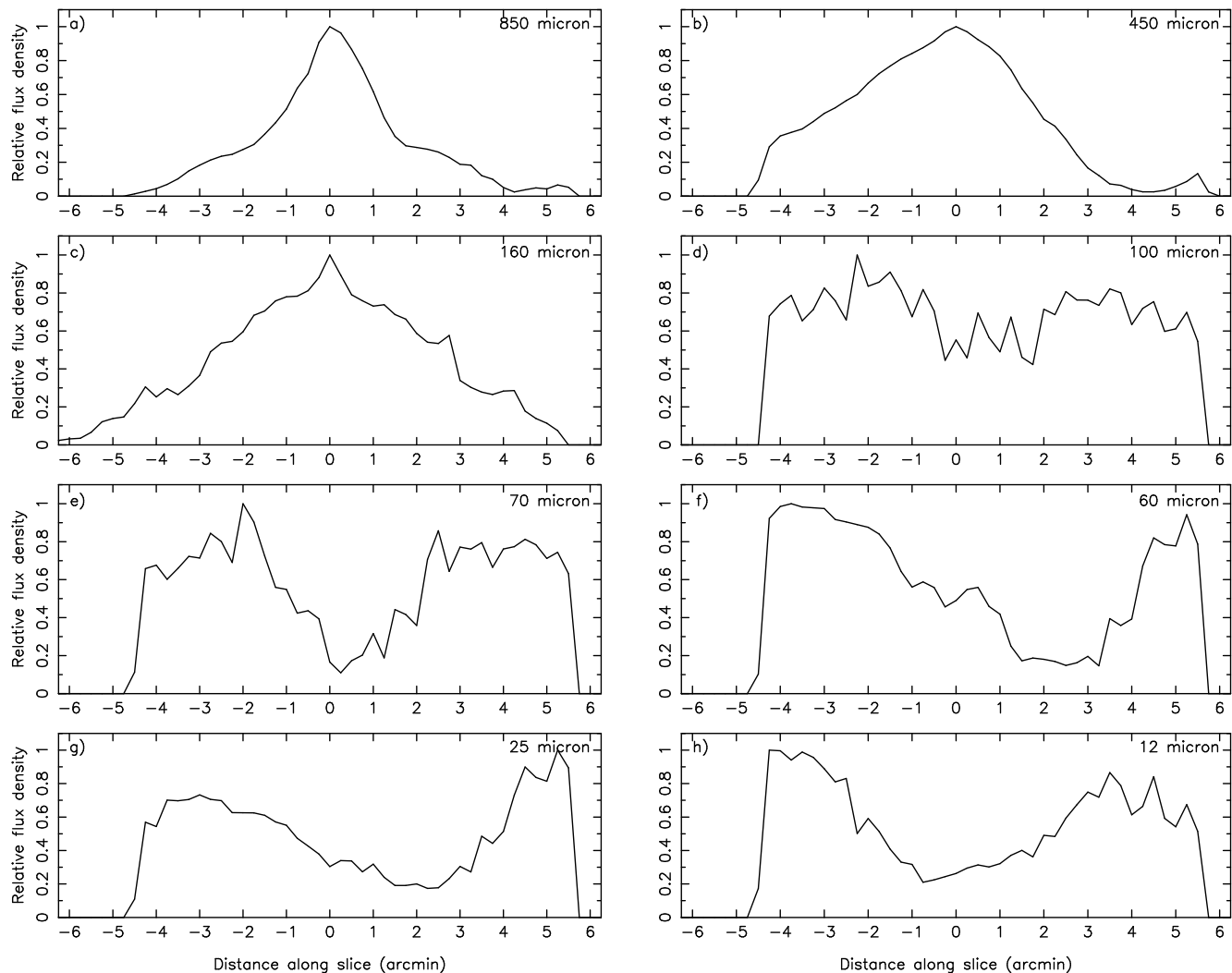


**Figure 4.** One-dimensional cuts through the data perpendicular to the filament at each of the eight wavelengths studied. Each cut has been normalised to its own peak.

The LEOPARD software tool (LEOPARD 2005) was used to search the Spitzer data archive for MIPS scan-map data coincident with the position of the SCUBA data. 160- $\mu\text{m}$  unfiltered basic calibrated datasets 1122-6112/6368/6624/6880 from pipeline version S14.4 were identified and downloaded. The data were filtered to remove the frames taken directly after stimulator-flashes (calibration events that can leave bright residuals). The data were re-gridded with the MOPEX software package into an image with 15-arcsec-diameter pixels (Makovoz & Khan 2005). This image was then iteratively cleaned and filled to reject spurious pixel artefacts as described in Kirk, Ward-Thompson, & André (2007).

Rather than process the 70- $\mu\text{m}$  data ourselves we have made use of data released by this Legacy Project. These data come from the same original dataset, but have been processed to an enhanced level by the Legacy Project team. The data were originally reduced with pipeline version S11.1, and finally smoothed to the same 40-arcsec resolution as the 160- $\mu\text{m}$  data.

The chopping that is employed by the JCMT to remove the effects of the atmosphere also has the effect of limit-

ing the sensitivity to spatial scales larger than a few times the largest chop throw. Spitzer does not need to chop, and so does not suffer from this. In order to directly compare the MIPS and SCUBA data, synthetic chops with the same properties as the SCUBA chops were added to the MIPS data using the *SURF* routine *ADD\_DBM*. These chops were then removed using the same method as that employed for the SCUBA data. The SCUBA and MIPS data therefore have the same angular resolution, and are sensitive to structures on the same spatial scales and can thus be compared directly.

### 2.3 IRAS Data

The Infrared Astronomical Satellite (IRAS; Wheelock et al. 1994) was a 60-cm space-borne telescope which carried out all-sky surveys at 12, 25, 60 and 100  $\mu\text{m}$ . IRAS had an angular resolution of 20, 20, 60 and 120 arcsec respectively at the four wavelengths. IRAS data for TMC1 were retrieved from the IRAS archive using the *skyview* interface (McGlynn, Scollick, & White 1998). In order to remove large scale gradients which were present in the IRAS data,

they were smoothed using a 5-arcmin Gaussian function. This smoothed map was subsequently subtracted from the data, thus removing the large-scale structure, and also making the data directly comparable with the chopped data.

### 3 RESULTS

Figures 3(a)–(d) show the bull’s tail at 850, 450, 160 and 70  $\mu\text{m}$  respectively. The three long wavelength maps show the filament in emission, whereas the 70  $\mu\text{m}$  map shows the filament in absorption against the warmer background of the surrounding cloud. This is therefore clearly a dense structure, for it to be seen in absorption at a wavelength as long as 70  $\mu\text{m}$ .

Figure 3 shows that the filament is much narrower at 850 than at 450 or 160  $\mu\text{m}$ . In addition, the absorption at 70  $\mu\text{m}$  is also very narrow, and matches quite well to the 850- $\mu\text{m}$  emission. We interpret this as the filament having a cold dense inner region, where the extinction is the highest, surrounded by a warmer, less dense outer ‘jacket’. This is explored further in Section 4.1.

Figure 4 shows a series of one-dimensional cuts through the data of Figure 3, in a direction perpendicular to the long axis of the filament. In addition, Figure 4 shows the equivalent cuts through the IRAS data at 12, 25, 60 & 100  $\mu\text{m}$ . Figure 4 shows that there is a transition at approximately 100  $\mu\text{m}$ , longward of which the filament is seen in emission. At wavelengths shorter than 100  $\mu\text{m}$  the filament is seen in absorption. At 100  $\mu\text{m}$  there is a hint that the filament is seen in absorption, although the data are quite noisy. Figures 4(a)–(c) also confirm that the filament is narrower at 850  $\mu\text{m}$  than at 450 or 160  $\mu\text{m}$ . We investigate this effect in Section 4.1.

## 4 ANALYSIS

### 4.1 Empirical Model

Figure 5 shows the 850- and the 160- $\mu\text{m}$  profiles overlaid. The two profiles have been normalised to a blackbody with a temperature of 12 K. To do this, the observed 850- and 160- $\mu\text{m}$  profiles were divided by the flux-density which would be emitted by a 12 K blackbody with a 160- $\mu\text{m}$  flux-density equal to the observed value at the filament centre. The two profiles would have the same peak value of 1 if the data were due to a single emitting source at 12 K. We use a blackbody function in this instance, as it has fewer free parameters than the modified blackbody used in Section 4.2.

In the outer parts of the filament, there is quite a good agreement between the two profiles, indicating that the same dust is emitting at both wavelengths, and that the 850- $\mu\text{m}$  data also match this model quite well in the ‘shoulders’ of the profile. However, there is an excess of emission at 850  $\mu\text{m}$  in the centre of the profile. This shows that there is a second dust component in the centre of the filament which is colder than 12 K, which therefore emits more strongly at 850  $\mu\text{m}$ . In Section 5 we discuss specific models of the filament, but first we attempt a simple spectral energy distribution (SED) analysis of the two components.

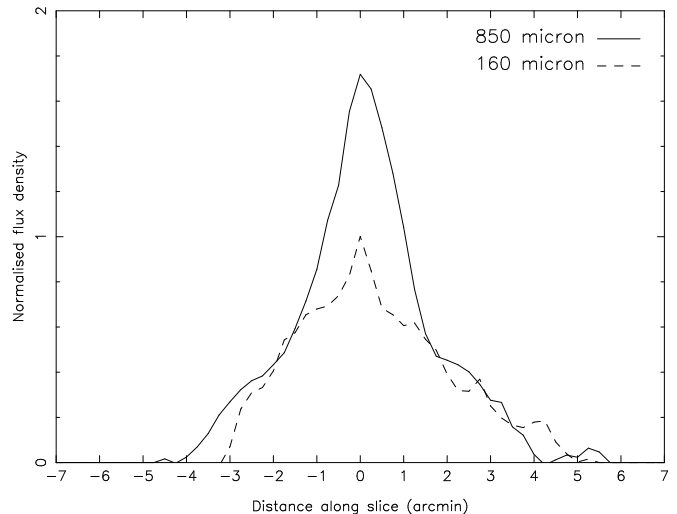


**Figure 5.** The 850- and 160- $\mu\text{m}$  cuts normalised to a 12-K blackbody (see text for details). Note that the two curves match up well in the ‘shoulders’ of the two profiles, but that the 850- $\mu\text{m}$  data have an additional narrow component of extra emission on the peak of the filament.

### 4.2 Temperature Analysis

We measured the total flux density from the filament at each of the three wavelengths in which it is seen in emission. We also separated out the flux density of the central component from that of the outer shoulder, or jacket, by fitting two components to the various profiles, such as those seen in Figure 5.

Figure 6(a) shows the flux densities of the filament centre (solid squares) and the outer shoulder (hollow squares) together with two modified blackbody fits to the data in the normal manner (see, e.g. Ward-Thompson, André, & Kirk 2002). Following Kirk, Ward-Thompson, & André (2007), the parameters  $\beta$  and the critical wavelength ( $\lambda_c$ ) are constrained to be equal to 2 and 50  $\mu\text{m}$  respectively. The best fits to the data are found to be 12 K for the outer filament, and 9 K for the filament centre.

We assume when we look along a line of sight towards the centre of the filament, that as well as the cold central filament, we also see the outer component (in front of, and behind the central filament). Therefore, to model the emission from the central component, we must also take account of the outer component. Hence we must fit a two-temperature SED to the emission from the central component.

Figure 6(b) shows the flux densities of the central component of the filament fitted by two modified blackbodies. We constrain the warmer component to be 12 K, as discovered in Figure 6(a), and fit the residual emission with a second component. In this way we find that the best fit temperature for the cold dust is actually 8 K. The resulting two-part SED is plotted on Figure 6(b). Hence we see that the best fit to the data from a simple two-component SED analysis is for a central cold filament at 8 K, surrounded by a broader and warmer component at 12 K.

### 4.3 Comparison with previous work

Tóth et al. (2004) used the IRAS 60- and 100- $\mu\text{m}$  data, to-

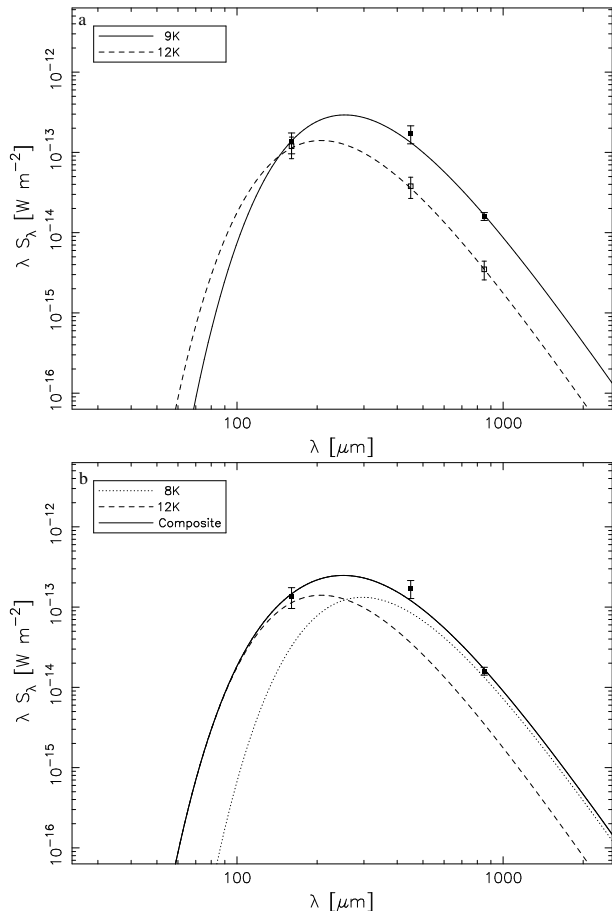


**Figure 6.** (a) Flux densities of the central component of the filament (filled squares) and the outer component (open squares) at each of the three wavelengths at which the filament is seen in emission. Spectral energy distribution fits in the form of modified blackbody curves are also shown for both the central filament (solid line – 9 K) and the outer filament (dashed line – 12 K). (b) Flux densities for the central component of the filament only. A two-component SED for the central part of the filament is also shown. The dashed line represents the same 12-K fit as before, but now the dotted line shows a fit to the residual flux densities at the two longer wavelengths, which corresponds to an 8-K modified blackbody. The solid line shows the sum of the two.

gether with 200- $\mu\text{m}$  data from the Infrared Space Observatory (ISO) to determine the temperature of TMC1-CP, which is roughly coincident with the filament that we are studying (see Figure 2).

They estimated a temperature of 11.4 K, which is consistent with the 12 K that we have measured in the outer part of the filament. Tóth et al. (2004) also found a similar temperature from studies of  $\text{NH}_3(1,1)$  and  $(2,2)$ . Stepnik et al. (2003) used the balloon-borne PRONAOS telescope to observe the L1506 cloud in Taurus (see Figure 1). They measured a temperature of 12.1 K.

Schnee et al. (2007) observed the TMC1-C region using SCUBA data at 450 and 850  $\mu\text{m}$  together with 1.2-mm data from the Institut de Radio Astronomie Millimétrique (IRAM) 30-m telescope. They found the temperature to be in the range of 6 – 16 K. All of these independent estimates are consistent with our findings.

#### 4.4 Column density

The measured values of the 850  $\mu\text{m}$  flux density at the centre of the filament and in its outer part are 0.082 Jy/beam and 0.022 Jy/beam respectively. The flux density of the outer part was measured 100 arcsec from the centre of the filament. From these measurements, together with the temperatures determined above, we can calculate the column density of material along the two lines of sight.

The mass per beam can be calculated using:

$$M_{beam} = \frac{S_{850} D^2}{\kappa_{850} B_{850,T}}, \quad (1)$$

where  $S_{850}$  is the 850  $\mu\text{m}$  flux density,  $D$  is the distance to the filament,  $\kappa_{850}$  is the mass opacity of the gas and dust, and  $B_{850,T}$  is the value of the blackbody function at a wavelength of 850  $\mu\text{m}$  at temperature  $T$ . We assume a distance to TMC1 of 140 pc (Elias 1978), and a mass opacity of  $0.01 \text{ cm}^2 \text{ g}^{-1}$  (see André, Ward-Thompson, & Barsony 1993; André, Ward-Thompson, & Motte 1996; Ward-Thompson, Motte, & André 1999, for a detailed discussion of both this value of  $\kappa_{850}$  in particular and of this method of obtaining masses in general).

The column density,  $N(\text{H}_2)$ , is then calculated using:

$$N(\text{H}_2) = \frac{M_{beam}}{2.8 m_H \pi r_{beam}^2}, \quad (2)$$

where  $r_{beam}$  is the radius of the beam at the distance of TMC1. This yields column densities of  $3.8 \times 10^{22} \text{ cm}^{-2}$  and  $4.4 \times 10^{21} \text{ cm}^{-2}$  for the central part and the outer part of the filament respectively. Hence we see that the centre of the filament has roughly an order of magnitude higher column density than the outer part.

We can also calculate the column density using the 70- $\mu\text{m}$  data, where the filament is seen in absorption, using the method described by Bacmann et al. (2000 – see also Ward-Thompson et al. 2006). This compares the measured intensity where the absorption is the strongest ( $I_{on}$ ), with the intensity off the filament ( $I_{off}$ ). A third measure ( $I_{fore}$ ) away from the region is also required to account for the zodiacal light and other foreground emission between us and the molecular cloud, as well as the large-scale background Galactic emission. The optical depth ( $\tau_\lambda$ ) of the filament is given by the following (Ward-Thompson et al. 2006):

$$e^{-\tau_\lambda} = \frac{I_{on} - I_{fore}}{I_{off} - I_{fore}}. \quad (3)$$

The column density is calculated using:

$$N(\text{H}_2) = \frac{\tau_\lambda}{\sigma_\lambda}, \quad (4)$$

where  $\sigma_\lambda$  is taken to be  $2.6 \times 10^{-24} \text{ cm}^2$  at 70  $\mu\text{m}$  (Draine & Lee 1984, see their figure 9). Measured values of  $I_{on}$ ,  $I_{off}$  and  $I_{fore}$  are 50.91, 51.13 and 49.51 MJys $^{-1}$  respectively, which lead to an estimate of the column density of  $5.6 \times 10^{22} \text{ cm}^{-2}$ . This is very close to the value of  $3.8 \times 10^{22} \text{ cm}^{-2}$  calculated above from the 850- $\mu\text{m}$  data in emission. The fact that two different data-sets from two different telescopes, and two different methods of calculation, give essentially the same answer give added confidence to our estimates.

## 5 RADIATIVE TRANSFER MODELLING

In this section we employ more sophisticated techniques to model all of the data, in order to understand the density structure of the filament in more detail. We use a radiative transfer code (Stamatellos & Whitworth 2003) to model the data, using a variety of parameter values to obtain the best fit simultaneously at all wavelengths. In each case, the filament is approximated by a cylinder, which is heated externally by the interstellar radiation field (ISRF). To determine the properties of the filament a large number of radiative transfer simulations were performed, and a best-fit solution was found.

We assume that the dust consists of carbonaceous and silicate grains with size distribution from Weingartner & Draine (2001). These properties are appropriate for the dust in the ISM ( $R_V = 3.1$ ; see Draine 2003).

### 5.1 Monte Carlo radiative transfer

The radiative transfer calculations were performed using PHAETHON, a 3D Monte Carlo radiative transfer code developed by Stamatellos & Whitworth (2003). The code uses a large number of monochromatic luminosity packets ( $L$ -packets) to represent the radiation sources in the system. The  $L$ -packets are injected into the cloud and interact (are absorbed, re-emitted, scattered) stochastically with it.

If an  $L$ -packet is absorbed its energy is added to the local region and raises the local temperature. To ensure radiative equilibrium the  $L$ -packet is re-emitted immediately with a new frequency chosen from the difference between the local cell emissivity before and after the absorption of the packet (Bjorkman & Wood 2001; Baes et al. 2005). For more details, see Stamatellos & Whitworth (2003).

We modelled the filament using a symmetric cylinder, and hence the code used here is optimised for the study of systems with axial symmetry. The filament is typically divided into  $\sim 4000$  cells. The number of cells used is chosen such that the density and temperature differences between adjacent cells are small.

### 5.2 Heating of the filament

Our simple modelling above has shown us that the centre of the filament is colder than the outer parts. Thus we deduce that there are no heating sources embedded within the filament, and hence the filament is starless. In order to verify this, Spitzer MIPS 24  $\mu\text{m}$  and Spitzer IRAC data for the filament were searched for YSOs and protostars (c.f. Allen et al. 2004; Harvey et al. 2007; Rebull et al. 2007). With the exception of a single class I source coincident with the outskirts of the filament, there are no observed internal heating sources. The only heating source considered is therefore the interstellar radiation field (ISRF). For this radiation field we adopt a revised version of the Black (1994) interstellar radiation field (BISRF). The BISRF consists of radiation from giant stars and dwarfs, thermal emission from dust grains, cosmic background radiation, and mid-infrared emission from transiently heated small PAH grains (André et al. 2003).

This radiation field is modulated by the ambient cloud around the filament. Hence the incident radiation field on

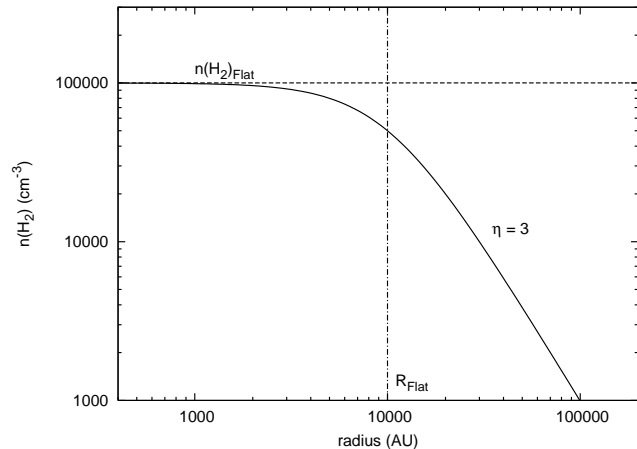


**Figure 7.** A Plummer-like analytic density profile, with  $n(H_2)_{flat} = 10^5 \text{ cm}^{-3}$ ,  $R_{flat} = 10^4 \text{ AU}$  and  $\eta = 3$ .

the filament is enhanced at FIR and longer wavelengths, and attenuated at shorter wavelengths. The  $L$ -packets representing the ambient radiation field (typically a few  $10^{10}$  packets) are injected from the outside of the virtual ambient cloud surrounding the filament with injection points and injection directions chosen to mimic an isotropic radiation field.

### 5.3 Plummer-like geometry

The geometry we assume is a cylinder with a Plummer-like density profile (Plummer 1911). So we use axial symmetry with the density being approximately flat in the centre of the filament and dropping as a power-law in the envelope of the filament, according to the Plummer relation:

$$n(H_2)(r) = n(H_2)_{flat} \left[ \frac{R_{flat}}{(R_{flat}^2 + r^2)^{1/2}} \right]^\eta, \quad (5)$$

where  $r$  is the distance from the axis of symmetry of the cylinder,  $n(H_2)_{flat}$  is the density at the axis of symmetry,  $R_{flat}$  is the extent of the region in which the density is approximately uniform, and  $\eta$  is the power-law slope at large values of  $r$ . This analytic form is illustrated in Figure 7. The filament is surrounded by a virtual ambient cloud, which has a uniform density  $n(H_2)_{amb}$ . The role of this cloud is to modify the ambient radiation field that heats the filament externally.

We use the term *Plummer-like* because a true Plummer profile has  $\eta = 5$ , whereas we treat this as a free parameter. A Plummer-like profile was selected because it provides a high-density inner region, which decreases to large radii, with a small number of parameters. The model can produce images of the source at any requested wavelength, convolved to any resolution. From these images we can produce one-dimensional cuts perpendicular to the cylinder for comparison with the data.

Whitworth & Ward-Thompson (2001) used a Plummer-like profile to model prestellar cores as they collapse to form protostars. They found that this model successfully predicted both the observed infall rates, and the relative lifetimes of the different evolutionary stages.

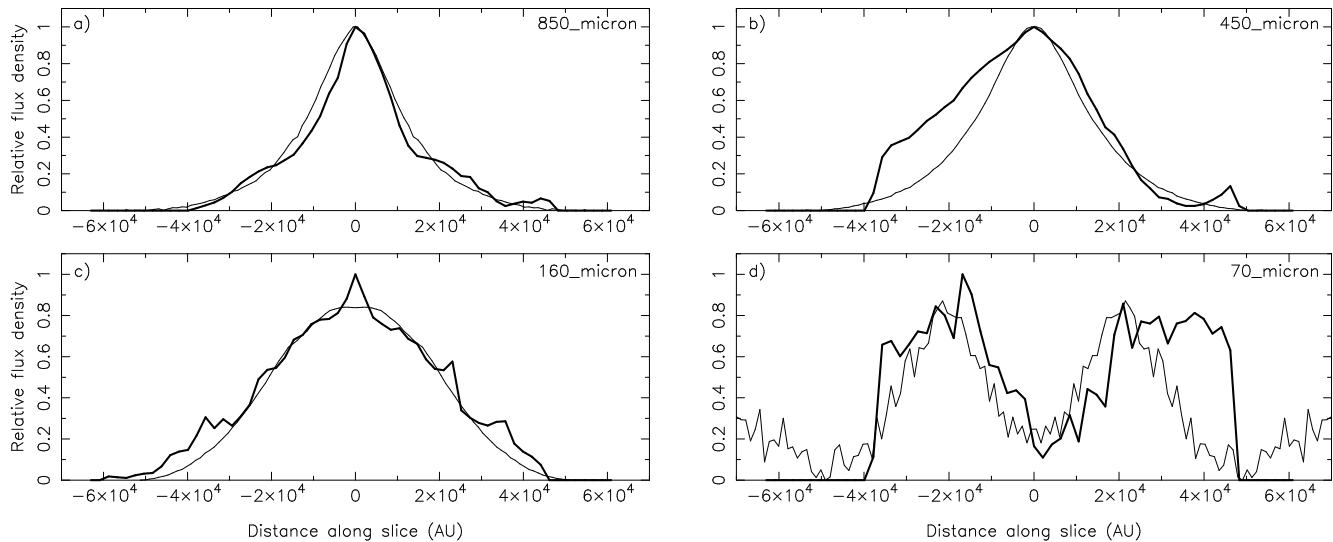


**Figure 8.** The cuts through the data from Figure 4 (bold lines), with overlaid (thin lines) the best fit profiles from the radiative transfer model.

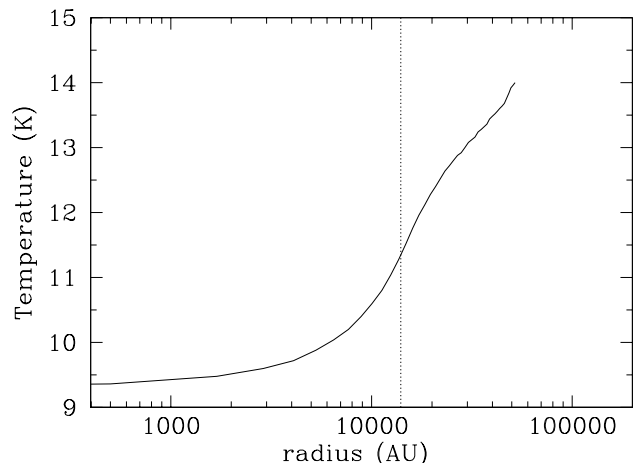
The following parameter space was explored.  $R_{flat} = 5 \times 10^2 - 1.5 \times 10^4$  AU,  $n(H_2)_{flat} = 7 \times 10^4 - 2 \times 10^7$  cm $^{-3}$ ,  $\eta = 1 - 4$ . In addition, the filament was embedded in a diffuse medium, with a visual extinction varying from  $A_V = 0.01 - 0.55$ .

Figure 8 shows the best-fit results for this model. The cuts through the model filament are compared to those through the data (see Figure 4). The parameters for this model are  $R_{flat} = 10^4$  AU,  $n(H_2)_{flat} = 1.75 \times 10^5$  cm $^{-3}$ ,  $\eta = 3$  and  $A_V$  in the external cloud equal to 0.39. The IRAS data are not included in this figure as they are of insufficient quality for detailed modelling at this scale.

This model shows a good fit to the filament in emission at 850 and 160  $\mu$ m, and fits one side of the asymmetric profile of the filament at 450  $\mu$ m. The model also shows the filament in absorption at 70  $\mu$ m. While this is not necessarily a unique fit to the data, it shows that the filament can be modelled with a fairly simple geometry and uniform grain properties throughout.

This is in contrast to the result of Stepnik et al. (2003), who need to invoke a non-uniform grain distribution in order to fit the far-infrared density profiles of a similar filament in Taurus. Stepnik et al. conclude that grain aggregation is important in the central  $3 \times 10^4$  AU, and is required to model the emission. We can explain the emission from our filament without a need for a change in grain properties.

The radiative transfer model allows us to measure the temperature of the dust grains as a function of position. This temperature does not vary with grain size, but is the same for all grains at a specific position. The temperature profile of the best-fit model is shown in Figure 9. This gives us an independent temperature estimate for comparison with the SED fitting carried out in Section 4.2. The model predicts a temperature of 12 K for the outer component of the filament, in agreement with the temperature determined from the SED fits. The central temperature is slightly higher than the best fit SEDs (9.8 K compared to 8 – 9 K).



**Figure 9.** The temperature profile from the best-fit model. The vertical dotted line shows the radial distance of the outer component of the filament (see section 4.2.)

## 6 CONCLUSIONS

We have presented submillimetre data from SCUBA on the JCMT and far-infrared data taken by Spitzer and IRAS, for a filament in TMC1 which we have named the bull’s tail. TMC1 is the densest part of the Taurus molecular cloud region. The filament is seen in emission at all wavelengths longer than 100  $\mu$ m, and in absorption at all shorter wavelengths.

The filament is significantly narrower at 850  $\mu$ m, which we attribute to a narrow, dense inner filament, running through the centre of the broader and warmer main filament. We have shown intensity cuts through the filament at wavelengths of 850, 450, 160, 100, 70, 60, 25 and 12  $\mu$ m, which are consistent with this scenario.

We have fitted SEDs to both the inner and outer components of the filament and find that the temperature decreases from 12 K in the outer part to 8 K at the centre. We

then used a radiative transfer code to fit the profile of the filament. We modelled the filament using a Plummer-like density profile with constant grain parameters throughout, and find good fits to all wavelengths.

## ACKNOWLEDGEMENTS

The authors would like to thank S. Schnee for helpful comments on this manuscript. This research is based on observations obtained with the James Clerk Maxwell Telescope, which is operated by the Joint Astronomy Centre in Hilo, Hawaii on behalf of the parent organizations STFC in the United Kingdom, the National Research Council of Canada and The Netherlands Organization for Scientific Research. The data were obtained using the Canadian Astronomy Data Centre, which is operated by the Herzberg Institute of Astrophysics, National Research Council of Canada. The observations were taken under the programs M98BI19, M98BC14, M99BC30, M01AI05, M01BC30, M01BN13 and M04BN16. This work is also based on observations made with the Spitzer Space Telescope, which is operated by the Jet Propulsion Laboratory, California Institute of Technology under a contract with NASA. We acknowledge the use of NASA's *SkyView* facility (<http://skyview.gsfc.nasa.gov>) located at NASA Goddard Space Flight Center. DN, JMK and DS acknowledge STFC for PDRA support.

## REFERENCES

- Allen L. E., et al., 2004, *ApJS*, 154, 363  
 Allen L. E., et al., 2007, in prep  
 André P., Ward-Thompson D., Barsony M., 1993, *ApJ*, 406, 122  
 André P., Ward-Thompson D., Motte F., 1996, *A&A*, 314, 625  
 André, P., Bouwman, J., Belloche, A., & Hennebelle, P. 2003, in *Chemistry as a Diagnostic of Star Formation*, University of Waterloo, Canada. Eds. Charles L. Curry and Michel Fich. NRC Press, p. 127.  
 Archibald E. N., et al., 2002, *MNRAS*, 336, 1  
 Bacmann A., André P., Puget J.-L., Abergel A., Bontemps S., Ward-Thompson D., 2000, *A&A*, 361, 555  
 Baes M., Stamatellos D., Davies J. I., Whitworth A. P., Sabatini S., Roberts S., Linder S. M., Evans R., 2005, *NewA*, 10, 523  
 Ballesteros-Paredes J., Hartmann L., Vázquez-Semadeni E., 1999, *ApJ*, 527, 285  
 Bjorkman J. E., Wood K., 2001, *ApJ*, 554, 615  
 Black J. H., 1994, *ASPC*, 58, 355  
 Bontemps S., Ward-Thompson D., André P., 1996, *A&A*, 314, 477  
 Cambrésy L., 1999, *A&A*, 345, 965  
 Dobashi K., Uehara H., Kandori R., Sakurai T., Kaiden M., Umemoto T., Sato F., 2005, *PASJ*, 57, 1  
 Draine B. T., 2003, *ARA&A*, 41, 241  
 Draine B. T., Lee H. M., 1984, *ApJ*, 285, 89  
 Duchêne G., Bouvier J., Bontemps S., André P., Motte F., 2004, *A&A*, 427, 651  
 Elias J. H., 1978, *ApJ*, 224, 857  
 Elmegreen B. G., Scalo J., 2004, *ARA&A*, 42, 211  
 Emerson D. T., 1995, in *ASP Conf. Ser. 75, Multifield Systems for Radio Telescopes*, ed. D. T. Emerson & J.M. Payne (San Francisco: ASP), 309  
 Evans N. J., II, et al., 2003, *PASP*, 115, 965  
 Fukui Y., Mizuno A., Nagahama T., Imaoka K., Ogawa H., 1991, *MmSAI*, 62, 801  
 Goldsmith P. F., Tang Y., Brunt C., Heyer M., Narayanan G., Snell R., Li D., 2005, *prpl.conf*, 8268  
 Goodwin S. P., Whitworth A. P., Ward-Thompson D., 2004, *A&A*, 419, 543  
 Güdel M., Padgett D. L., Dougados C., 2007, *prpl.conf*, 329  
 Harvey P., Merín B., Huard T. L., Rebull L. M., Chapman N., Evans N. J., II, Myers P. C., 2007, *ApJ*, 663, 1149  
 Heiles C. E., 1968, *ApJ*, 151, 919  
 Holland W. S., et al., 1999, *MNRAS*, 303, 659  
 Jenness T., Lightfoot J.F., 2000, *Starlink User Note 216*, Starlink Project, CCLRC  
 Kirk J. M., Ward-Thompson D., André P., 2005, *MNRAS*, 360, 1506  
 Kirk J. M., Ward-Thompson D., André P., 2007, *MNRAS*, 375, 843  
 Lynds, B. T., *ApJS* 1962, , 7, 1  
 LEOPARD, 2005, *Leopard User's Guide v4.1*, Spitzer Science Centre, Caltech, Pasadena, CA  
 Makovoz D., Khan I., 2005, *ASPC*, 347, 81  
 McGlynn T., Scollick K., White N., 1998, *IAUS*, 179, 465  
 Motte F., André P., Neri R., 1998, *A&A*, 336, 150  
 Motte F., André P., 2001, *A&A*, 365, 440  
 Olano C. A., Walmsley C. M., Wilson T. L., 1988, *A&A*, 196, 194  
 Onishi T., Mizuno A., Kawamura A., Ogawa H., Fukui Y., 1996, *ApJ*, 465, 815  
 Onishi T., Mizuno A., Kawamura A., Tachihara K., Fukui Y., 2002, *ApJ*, 575, 950  
 Padoan P., Cambrésy L., Langer W., 2002, *ApJ*, 580, L57  
 Plummer H. C., 1911, *MNRAS*, 71, 460  
 Rebull L. M., et al., 2007, *ApJS*, 171, 447  
 Rieke G. H., et al., 2004, *ApJS*, 154, 25  
 Sandell G., 1994, *MNRAS*, 271, 75  
 Schnee S., Kauffmann J., Goodman A., Bertoldi F., 2007, *ApJ*, 657, 838  
 Stamatellos D., Whitworth A. P., 2003, *A&A*, 407, 941  
 Stepnik B., et al., 2003, *A&A*, 398, 551  
 Tóth L. V., Haas M., Lemke D., Mattila K., Onishi T., 2004, *A&A*, 420, 533  
 Ungerechts H., Thaddeus P., 1987, *ApJS*, 63, 645  
 Ward-Thompson D., Chini R., Krugel E., Andre P., Bontemps S., 1995, *MNRAS*, 274, 1219  
 Ward-Thompson D., Motte F., André P., 1999, *MNRAS*, 305, 143  
 Ward-Thompson D., Kirk J. M., Crutcher R. M., Greaves J. S., Holland W. S., André P., 2000, *ApJ*, 537, L135  
 Ward-Thompson D., André P., Kirk J. M., 2002, *MNRAS*, 329, 257  
 Ward-Thompson D., Nutter D., Bontemps S., Whitworth A., Attwood R., 2006, *MNRAS*, 369, 1201  
 Weingartner J. C., Draine B. T., 2001, *ApJ*, 548, 296  
 Werner M. W., et al., 2004, *ApJS*, 154, 1  
 Whitworth A. P., Ward-Thompson D., 2001, *ApJ*, 547, 317  
 Wheelock S. L., et al., 1994, *STIN*, 95, 22539